COLLABORATIVE HIRENASD ANALYSES TO ELIMINATE VARIATIONS IN COMPUTATIONAL RESULTS

Pawel Chwalowski and Jennifer Heeg[1], Mats Dalenbring and Adam Jirasek[2], Markus Ritter[3], and Thorsten Hansen[4]

[1]Aeroelasticity Branch, NASA Langley Research Center, Hampton, VA 23681, USA
Pawel.Chwalowski@nasa.gov, Jennifer.Heeg@nasa.gov

[2]Division for Information and Aeronautical Systems
Swedish Defense Research Agency (FOI), SE- 164 90 Stockholm, Sweden
Mats.Dalenbring@foi.se, Adam.Jirasek@foi.se

[3]Institute of Aeroelasticity, German Aerospace Center (DLR),
Bunsenstraße 10, 37073 Göttingen, Germany
Markus.Ritter@dlr.de

[4]ANSYS Germany GmbH, Staudenfeldweg 12, 83624 Otterfing, Germany
Thorsten.Hansen@ansys.com

Abstract: In this paper, the post Aeroelastic Prediction Workshop (AePW) analyses considering HIgh REynolds Number AeroStructural Dynamics (HIRENASD) configuration are presented. The AePW took place in 2012 and the HIRENASD wind-tunnel model was tested in the European Transonic Windtunnel in 2006 by Aachen University′s Department of Mechanics with funding from the German Research Foundation. The computational results are obtained using TAU, Edge, Fluent, and FUN3D software using a common-grid approach, the same turbulence model, and the same post-processing methods. The results are obtained at Mach 0.8 for a Reynolds number of 7 million based on chord at three levels of grid refinement and include aerodynamic coefficients and coefficient of pressure obtained for steady-state or static aeroelastic equilibrium and for unsteady flow due to modally-excited wing. Both, the coefficient of pressure and the frequency response functions, are compared against the AePW computational database and the experimental data. The common-grid analyses approach with the same turbulence model and the same post-processing methods brings the computational results obtained by four solvers closer together when compared to the AePW database. However, this approach does not bring the computational results closer to the experimental data.

1 INTRODUCTION

The Aeroelastic Prediction Workshop (AePW) [1] took place in conjunction with the 53rd AIAA Structural Dynamics and Materials Conference on April 21-22, 2012, in Honolulu, Hawaii. The primary purpose of the AePW was to take a first step in assessing the state of the art in computational aeroelasticity. The approach was to challenge the computational community to analyze the same configurations and to present their results at the workshop. The secondary purpose of the workshop was to establish a benchmarking standard for use in validating the accuracy of computational aeroelasticity codes. Currently, such

a benchmarking standard does not exist in analysis of unsteady aerodynamic phenomena and the corresponding effects on the response of the structure. And, the third purpose of the AePW was to identify the path forward.

The AePW challenged the community to analyze three configurations. The first two configurations involved rigid geometries with static and/or forced motion boundary conditions with attached and transiently separated flows at transonic conditions. The first configuration utilized the NASA Rectangular Supercritical Wing (RSW), which was tested in the NASA Langley Transonic Dynamics Tunnel (TDT) in 1982. For this experiment, a rectangular-planform, supercritical wing was sidewall-mounted to a small splitter plate and oscillated in pitch, exhibiting a small amount of shock-induced separated flow at high angle of attack. The second configuration utilized the NASA Benchmark Supercritical Wing (BSCW), which similarly had a rectangular planform and was sidewall-mounted. Tested in 2000, the BSCW was mounted on a large splitter plate assembly and oscillated in pitch via the TDT Oscillating Turntable (OTT). Separated flow was observed from the shock foot to the trailing edge of the wing at a moderate (five degrees) angle of attack.

Both the RSW and BSCW were treated as rigid wings for the AePW. The models were designed and tested such that their structural modes were well separated from the frequencies of oscillation. The rigid treatment of these configurations at the AePW test points has been demonstrated to be appropriate by Heeg [2,3].

The third configuration, the HIRENASD model, was tested in the European Transonic Windtunnel (ETW) in 2006. For this experiment, a stiff, semi-span, transport-type wing configuration was mounted to the tunnel ceiling and oscillated at or near the frequency of the first bending mode, the second bending mode, and the first torsion mode.

The format of the AePW was modeled based on other workshops. Excellent examples of code validation in the international community assuming steady aerodynamics are the series of five AIAA Drag Prediction Workshops (DPWs) [4] that have been held since 2001 and the AIAA High Lift Prediction Workshop (HiLiftPW) [5] that was held in 2010. These workshops had three main objectives. The first was to assess the ease and practicality of using state-of-the-art computational methods for aerodynamic load prediction. The second was to impartially evaluate the effectiveness of the Navier-Stokes solvers, and the final objective was to identify areas for improvement. The structure of the DPW and the HiLiftPW provided a template for the AePW.

The conclusion from the first three DPW workshops was that, as stated by Morrison and Hemsch [6], "After three workshops, it is still clear that grids remain a first order effect and obtaining high quality grids is the first step to obtaining a high quality solution. Furthermore, obtaining a high quality family of grids for relatively simple wing-body configurations suitable for grid convergence studies remains a formidable challenge. Software tools to develop a family of grids rather than a single grid would provide an immense improvement in the CFD process." The fourth DPW sought to improve on grid generation based on above statement, however, Park [7] quotes that "The variation of computed lift and pitching moment between flow solvers grew dramatically between 3 and 4 degrees angle of attack for DPW-IV." For the DPW-V, the organizing committee provided a common grid to be utilized by structured and unstructured grid flow solvers to further reduce the influence of the grid on solutions.

The majority of the AePW workshop participants built their own grids of the HIRENASD configuration. Specifically, only three out of 14 analyses teams used grids provided by other AePW teams. Participants conducted analyses using their CFD software with their choice of turbulence model, number of mode shapes in fluid-structure coupling analysis, and they post-processed their dynamic data using their own software to calculate the frequency response functions of pressure due to wing displacement. In this paper, we are presenting the results of HIRENASD configuration re-analysis using a common grid approach and the same turbulence model, specifically the Spalart-Allmaras one equation model [8]. In addition, in case of the modal structural solvers, the same number of mode shapes, 30, was used in fluid-structure coupling analysis. Finally, the dynamic results are post-processed using the same software to produce the frequency response functions. The above process shows the effect of these constraints on the computational results and compares these results to the existing AePW computational database. This paper does not show the influence of each constraint individually, but rather treats these constraints as a group.

Information relevant to the HIRENASD configuration will be presented first. Details associated with the numerical software employed will be presented next. The Finite Element Model (FEM), computational grid and post processing methods are then discussed. Finally, comparison of the computational results: rigid body, static aeroelastic and forced motion, will then be presented. Four flow solvers, TAU, Edge, Fluent, and FUN3D are used to compare rigid body and static aeroelastic solutions. Three flow solvers, TAU, Edge, and FUN3D are used to compare forced motion results. The Fluent solver dynamic results were not obtained in time for this publication and will be published in the future.

2 HIGH REYNOLDS NUMBER AERO-STRUCTURAL DYNAMICS (HIRENASD) PROJECT

The HIRENASD Project was led by RWTH Aachen University's Department of Mechanics with funding from the German Research Foundation. HIRENASD was initiated in 2004 to produce a high-quality transonic aeroelastic data set at realistic flight Reynolds numbers for a large transport-type wing/body configuration and was tested in the European Transonic Windtunnel (ETW) in 2006. The HIRENASD wing planform, shown in Figure 1a, is a ceiling-mounted, semi-span, clean-wing configuration with a leading-edge sweep of 34 degrees, a span of approximately 1.3 meters, and a mean aerodynamic chord of 0.3445 meters. It consists of three wing sections. The two outboard sections use an 11%-thick BAC3-11/RES/30/21 supercritical airfoil. The inboard section uses the same airfoil thickened linearly from 11% at its outer edge to 15% at the root. To minimize boundary-layer interference during testing, a generic fuselage was included. It extended 0.09 meters from the tunnel ceiling and was mechanically isolated from the wing by a labyrinth seal. Boundary-layer transition strips were affixed to the upper wing surface at 12-15% chord and to the lower surface at 5% chord for portions of the test. Extensive measurements were acquired during testing of the HIRENASD model. Instrumentation included a six-component balance, surface pattern tracking (SPT) optical markers for surface deformation measurements on the pressure side of the wing, 11 accelerometers, 28 strain gages, and 259 unsteady pressure transducers. The pressure transducers were distributed along the upper and lower surfaces at the seven span stations shown in Figure 1b.

The HIRENASD test matrix consisted of both static and dynamic measurements acquired at different flow conditions, with variations of Reynolds number from 7 million up to 73 million based on the mean aerodynamic chord and dynamic pressures up to 130,000 Pascals at six transonic Mach numbers: 0.70, 0.75, 0.80, 0.83, 0.85, and 0.88. The test medium at ETW was nitrogen. For static testing, pressure distribution and lift and drag coefficients were acquired during angle-of-attack polars, where the angle of attack was slowly varied at an angular sweep rate of 0.2 degrees per second, holding all other operational parameters constant. Dynamic testing involved forced oscillations of the wing via differential forcing at or near one of three of the wing's natural frequencies: the first bending mode at approximately 27 Hz, the second bending mode at approximately 79 Hz, or the first torsion mode at approximately 265 Hz.

For AePW, six test cases were selected for the HIRENASD computational challenge, as shown in Table 1, differentiated by the Mach number, angle of attack, and Reynolds number. Three steady (static aeroelastic) cases were chosen (Table 1: Cases 1, 2, and 5) and second bending mode frequency oscillation cases at the corresponding test conditions (Table 1: Cases 3, 4, and 6). For workshop test cases at $Re_c = 7.0$ million, the boundary layer transition strips were affixed to the upper surface of the wing at 12-15% chord and on the lower surface at 5% chord.

In this paper, we will focus on comparing HIRENASD experimental data from test No. 159 (Test Case 3 in Table 1) with computational results. In the test No. 159 the HIRENASD model was excited close to the second bending mode frequency. The static aeroelastic results are compared first against the corresponding experimental data, and finally, the forced excitation computational results will be compared against experimental data.

Table 1: HIRENASD Analysis Test Cases.

| Test Case	Mach No.	Mean α (deg)	Forcing Freq. (f, Hz)	Modal Amp. at Accel. 15 (m)	Reduced Freq. ω c / $2V_\infty$	Re_c *10^6	ETW Test No.
1	0.8	1.5	0	0	0	7	159
2	0.8	-1.34	0	0	0	23.5	271
3	**0.8**	**1.5**	**78.9**	**0.0024**	**0.333**	**7**	**159**
4	0.8	-1.34	80.4	0.0009	0.396	23.5	271
5	0.7	1.5	0	0	0	7	155
6	0.7	1.5	79.3	0.0020	0.378	7	155

3 FLOW SOLVERS

The four Reynolds-averaged Navier-Stokes (RANS) solvers used in this study are TAU [9, 10] from DLR, Edge [11] from FOI, Fluent from ANSYS [12], and FUN3D [13] from NASA. The brief description of each software relevant to the HIRENASD analysis is provided below.

3.1 TAU Code

The DLR TAU code is a collection of modules and libraries for the numerical simulation of viscous and inviscid flows about complex geometries without any restrictions in
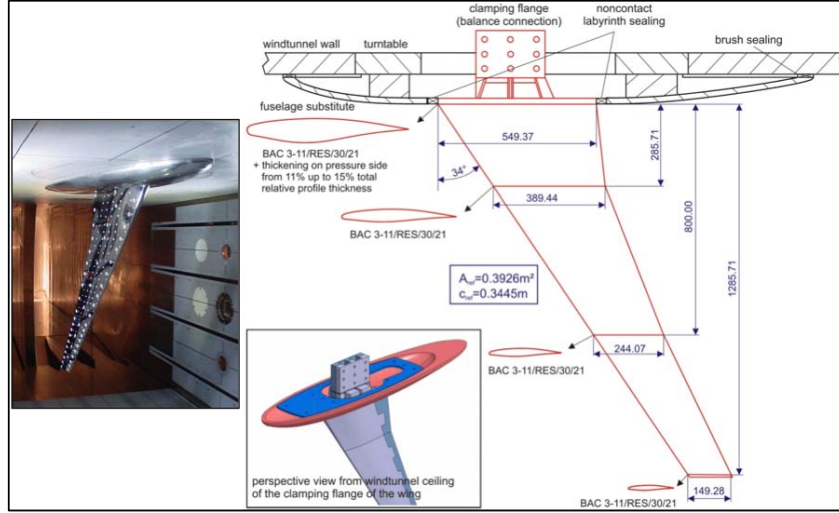
(a) HIRENASD wing model planform, assembly, and ETW installation photo. (Dimensions shown are in millimeters.)
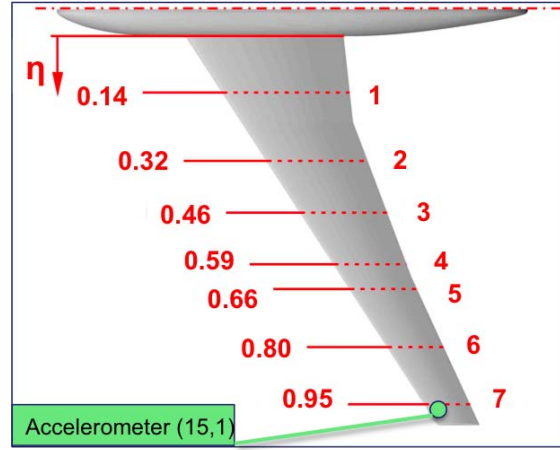
(b) HIRENASD experimental stations.

Figure 1: HIRENASD wing model planform and span stations 1-7 with accelerometer 15 location.

terms of Mach number. It employs hybrid, unstructured grids and uses an edge-based dual-cell approach (vertex centered scheme). User can choose from a range of turbulence models that properly fit their requirements. Time integration can be done with an explicit Runge-Kutta or an implicit lower-upper symmetric Gauss-Seidel (LU-SGS) scheme. For time accurate computations the dual-time stepping approach is employed. Different modules allow for enhanced functionalities of the TAU code: automatic grid partitioning, preprocessing, grid adaptation, grid deformation, overset grid techniques. The software has been validated extensively [9, 10].

Since weakly coupled aeroelastic simulations require a large amount of data transfer due to the different discretization methods used for the aerodynamic and the structural part, a framework has to be established for the efficient integration of the modules involved (aerodynamic solver, structural solver, grid deformation). The DLR flow solver was developed for an easy setup and running of multidisciplinary simulations and optimization

processes. It allows exchange of data between different numerical tools of different vendors and domains (such as non-linear optimization codes, aeroelasticity, aeroacoustics, etc.), where they can be combined easily in one workflow. The software design is completely object-oriented and based on Python interfaces to tie to third-party modules [14].

For all TAU static aeroelastic calculations presented here the modal approach was used to calculate structural deformations. This method allows a drastic reduction of the number of structural degrees of freedom that must be solved. Although the modal approach leads to a linear elastic model, this approach is justified since the overall structural deformations of the HIRENASD wing are small. Using a (mass-normalized) modal basis $\mathbf{\Phi}$ (obtained by an eigenvalue analysis), physical displacements $\vec{u}$ are related to generalized coordinates $\vec{q}$ as

$$\vec{u_s} = \mathbf{\Phi_s}\,\vec{q}\ , \tag{1}$$

where the subscript s denotes structural degrees of freedom.

The steady governing equation of a linear structure is given as

$$\mathbf{K}\,\vec{u_s} = \vec{f_s}\ , \tag{2}$$

and the same equation expressed in generalized coordinates becomes

$$\mathbf{\Omega}\,\vec{q} = \mathbf{\Phi_s^T}\,\vec{f_s}\ , \tag{3}$$

where $\mathbf{\Omega} = \mathbf{\Phi_s^T K \Phi_s}$, which for standard mode shape normalization produces a diagonal matrix containing the square of the system's natural frequencies.

The product of the transposed matrix of the mode shapes and the forces are the generalized forces. For weakly coupled aeroelastic systems, forces are obtained on nodes or cell centers of the aerodynamic grid and thus a transformation onto the structural nodes becomes necessary. Furthermore, structural deformations have to be mapped onto the aerodynamic grid. This data transfer can be realized in a linear fashion by a coupling matrix $\mathbf{H}$. Subscript a denotes aerodynamic data:

$$\vec{f_s} = \mathbf{H}^T\,\vec{f_a}\,,\vec{u_a} = \mathbf{H}\,\vec{u_s}\ . \tag{4}$$

The coupling matrix is built of radial basis functions, here a thin plate spline basis function was used. A simplification can be made by the interpolation of the mode shapes of the structural model onto the aerodynamic model in a preprocessing step:

$$\begin{aligned}
\vec{q} &= \mathbf{\Omega}^{-1}\,\mathbf{\Phi}_s^T\,\vec{f_s} \\
&= \mathbf{\Omega}^{-1}\,(\mathbf{H}\,\mathbf{\Phi}_s)^T\,\vec{f_a} \\
&= \mathbf{\Omega}^{-1}\,\mathbf{\Phi}_a^T\,\vec{f_a}\ .
\end{aligned} \tag{5}$$

Physical displacements are obtained directly on the aerodynamic grid by multiplication of $\mathbf{\Phi}_a$ with the generalized coordinates $\vec{q}$ calculated with equation 5:

$$\vec{u_a} = \mathbf{\Phi}_a\,\vec{q} \tag{6}$$

Matrix $\mathbf{\Phi}_a$ is referred to as the *aerodynamic mode shape matrix*. The use of this matrix avoids the time-consuming transformation of aerodynamic forces to structural forces and

the interpolation of structural deformations in every iterative step. This formulation is used for the static coupling simulations. In order to find the static aeroelastic equilibrium iteratively, several coupling steps are necessary. The convergence of the simulation can be accelerated by the use of a relaxation factor which scales the aerodynamic forces in the first coupling steps.

The unsteady HIRENASD wind-tunnel experiments were performed by exciting the wing in a structural eigenmode using a system of four piezoelectric stacks located near the wing root. Transferring this approach directly to the numerical simulation requires that the structural model must be excited at the same position as in the experiment using either physical or generalized forces with a prescribed frequency and magnitude. Particular attention must be paid to the magnitude of the forces to ensure the same amplitude of deformation of the wing as in the experiment. Several presentations of unsteady numerical simulation results of the HIRENASD model showed proper results with a forced motion approach [15]. This comparatively simple technique prescribes an elastic, time dependent deformation of the wing (mode shape) in an unsteady CFD calculation. No unsteady and time consuming fluid-structure coupling is performed. The maximum amplitude of the wing deformation (in terms of a generalized coordinate) as well as the frequency can be obtained by the experimental data. Using the nomenclature above, the time dependent deformation of the aerodynamic grid becomes:

$$
\begin{aligned}
\vec{u}_{a,x}(t) &= a_0 \, \boldsymbol{\Phi}_{a,x} \, sin\left(\omega\, t\right). \\
\vec{u}_{a,y}(t) &= a_0 \, \boldsymbol{\Phi}_{a,y} \, sin\left(\omega\, t\right). \\
\vec{u}_{a,z}(t) &= a_0 \, \boldsymbol{\Phi}_{a,z} \, sin\left(\omega\, t\right).
\end{aligned}
\tag{7}
$$

Where a_0 denotes the amplitude. A dual-time stepping scheme was used for all unsteady simulations. The calculations were stopped after a prescribed number of periods or convergence in the frequency domain.

3.2 Edge Flow Solver

The Edge [11] flow solver is a finite volume Navier-Stokes solver for unstructured grids. It employs an edge-based formulation which uses a node-centered method to solve the governing equations. It also employs local time-stepping, local low-speed preconditioning, multigrid and dual-time stepping for steady-state and time-dependent problems. It can be run in parallel on a number of processors to efficiently solve large flow cases. The convergence is enhanced by line implicit scheme [16].

For a very wide class of mechanical systems, the dynamics for small displacements can be accurately represented by a linear differential equation of the form

$$
M\ddot{x} + C\dot{x} + Kx = f,
\tag{8}
$$

where x is the vector of structural coordinates, and $f(t)$ is the corresponding vector of forces. The M, C, and K are the mass, damping and stiffness. The equation of motion can be reduced to the form,

$$
a_k\ddot{q}_k + 2\zeta_k a_k\omega_k\dot{q}_k + a_k\omega_k^2 q_k = Q_k, \quad k \in [1, N_m],
\tag{9}
$$

where ζ_k is the *damping ratio* for mode k and

$$
Q_k = \phi_k^T f,
\tag{10}
$$

is the corresponding generalized force. The structural damping matrix, C, is a linear combination of the mass and stiffness matrices M and K, i.e.. considered as a proportional or Rayleigh damping.

The transformation of the load/displacements from CFD grid to FEM elements and vice versa is done using a transformation matrix derived using the energy conservation condition.

3.3 ANSYS Fluent Solver

ANSYS Fluent is a conservative finite-volume method using a cell-centered control-volume method. It uses unstructured grids based on hexahedral, tetrahedral, prismatic, and polyhedral elements, as well as with combinations thereof. The convective transport terms in the conservation equations can be discretized with different methods. A second-order upwind differencing scheme was applied in the present study. Variable gradients are computed using a least square gradient method. The flux-difference splitting method of Roe is used to compute the inviscid flux vector [17]. ANSYS Fluent features pressure- and density-based solvers. In the present study the implicit density-based solver has been used. ANSYS Fluent solves the discretized momentum, mass and energy equations in an implicitly coupled manner. The coupled solution technique increases the robustness of the method. The coefficient matrices resulting from discretization are solved with an algebraic multi-grid technique (AMG). The resulting solution method is scalable, i.e. the computing time increases linearly with the number of grid nodes [12]. The discretization and solution steps are parallelized in a scalable manner using a domain decomposition method.

For the static aeroelastic analysis, ANSYS Mechanical and Fluent are applied to coupled structural and fluid flow domains in a sequential manner. The aerodynamic wing load resulting from the fluid flow simulations has been applied to a non-conformal structural grid using a conservative coupling method. The grid morphing tool RBF-Morph [18, 19] is used for updating the CFD grid based on the deformation calculated by ANSYS Mechanical. ANSYS Fluent and ANSYS Mechanical are both modules of the ANSYS Workbench software, which is a multi-physics environment enabling fluid-structure, fluid-thermal and other multi-physics couplings.

3.4 FUN3D Flow Solver

FUN3D is a finite-volume unstructured grid node-based mixed-element RANS flow solver. Various turbulence models are available, but as stated before, in this study the turbulence closure was obtained using the Spalart-Allmaras [8] one-equation model. Flux limitation was accomplished with the Venkatakrishnan [20] limiter scaled to the mean aerodynamic chord. Inviscid fluxes were computed using the Roe's flux-difference splitting scheme [17]. For the asymptotically steady cases under consideration, time integration was accomplished by an Euler implicit backwards difference scheme, with local time stepping to accelerate convergence. Most of the steady-state cases in this study were run for 10000 iterations to achieve convergence of integrated forces and moments to within $\pm 0.5\%$ of the average of their last 1000 iterations.

The dual-time stepping scheme with temporal error control is employed for the dynamic cases with grid deformation and forced motion [21]. At each global time step, the solution

is advanced in pseudo time based on a user-specified number of subiterations, or until the solution drops below the temporal error norm. The fraction of the temporal error norm used in this study was set to 0.05.

The grid deformation in FUN3D is treated as a linear elasticity problem. In this approach, the grid points near the body can move significantly, while the points further away may not move at all. For structural dynamics analysis, FUN3D is capable of being loosely coupled with an external finite element solver [22], or in the case of the linear structural dynamics used in this study, an internal modal structural solver can be utilized. This modal solver is formulated and implemented in FUN3D in a similar manner to other NASA aeroelastic codes (CAP-TSD [23] and CFL3D [24]).

The dynamic analysis was performed in a three-step process. First, the steady CFD solution was obtained on the rigid vehicle. Next, a static aeroelastic solution was obtained by continuing the CFD analysis in a time accurate mode, allowing the structure to deform. A high value of structural damping (0.99) was used to accelerate the solution to static aeroelastic equilibrium position with respect to the mean flow before the dynamic response was started. Finally, for the dynamic response, a user-specified modal motion was used. The modal displacement for mode n was computed as:

$$q_n = A_n sin(\omega_n t) \tag{11}$$

where A_n is amplitude, ω_n is frequency, and t is time. The time accurate cases presented here were run for four cycles before the surface pressure data were collected for another four cycles.

4 HIRENASD FINITE ELEMENT MODEL

The MSC Nastran^{TM} FEM of the HIRENASD configuration used for AePW is a modified version of the model provided by RWTH Aachen University [25]. The modifications include instrumentation masses, better bolt connections, and the ability to measure the deflections at the accelerometer locations. The result is a very detailed model, containing over 200,000 uniform solid hexagonal elements in the wing alone. Specific details of the FEM are described by Wieseman [26]. Normal modes analyses, called "solution 103", were performed on the modified FEM, and the first 30 modes were extracted and used in the aeroelastic analyses presented in this paper. Because the FEM external surface definition did not originally match the aerodynamic outer mold line (OML) an additional modification of the FEM was required. The FEM grid points were projected to the aerodynamic OML.

The fluid-structure coupling in the TAU, Edge, and FUN3D software is accomplished by modal structural solvers. This method requires the modes to be interpolated onto CFD surface mesh. To eliminate another source of differences among the computational results, the modes projected at DLR were used in the TAU, Edge and FUN3D computations. The FEM of HIRENASD is shown in Figure 2a. The second bending mode projected onto the CFD mesh including wing and fuselage is shown in Figure 2b. Here, the mode shape values were set to zero on the fuselage, with the exception of a very narrow region near the wing and the fuselage junction. This process eliminated a discontinuity in mode shape values at this junction, which had caused flow solvers to abort. Note, that as described

9

(a) Complete FEM of HIRENASD including mounting structure and excitation system.

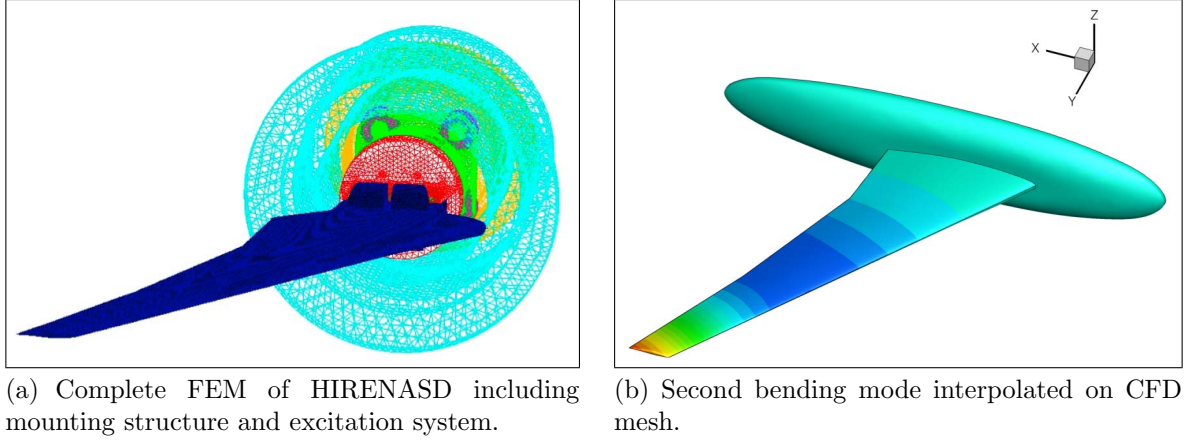(b) Second bending mode interpolated on CFD mesh.

Figure 2: FEM of HIRENASD and an example of the mode shape interpolation process from FEM into CFD surface mesh for the HIRENASD configuration.

earlier, the Fluent solver uses its own method of coupling fluid and structure for aeroelastic solutions.

5 COMMON CFD GRID

The flow domain was discretized using a hybrid grid composed of hexahedrons, prisms, tetrahedrons and pyramids. Based on an *IGES* definition of the geometry, the grid was built with the hybrid, quad-dominated grid generation software Solar [27]. The advantage of using unstructured quadrilateral elements rather than triangular elements on the wing and fuselage surfaces, is the drastic reduction in the number of cells required in the overall computational domain for comparable grid density.

Regions in the HIRENASD geometry where particular attention must be paid for the grid generation with respect to the expected flow conditions can be identified as follows:

- Wing-fuselage junction, in particular near the trailing edge
- Number of cells on the blunt trailing edge
- Wingtip near leading and trailing edge
- Discretization of the upper surface for shock resolution

The final CFD grid used for both the steady and unsteady simulations is characterized by the properties listed in Table 2. The grid on the symmetry plane, wing, wing's leading edge, and the wing tip for coarse, medium, and fine grid resolution is shown in Figure 3.

5.1 Post Processing

The dynamic comparison data selected for AePW consisted of magnitude and phase of the frequency response functions (FRFs). The frequency response functions of interest were the pressure coefficients (C_p) due to a selected displacement. The FRF for each pressure coefficient due to displacement was calculated at the principal frequency of the reference displacements.

Fourier domain analysis was performed on each dynamically-excited data set to produce FRFs for each pressure, relative to the displacement of the system. The FRFs were formed

Table 2: Solar grid statistics for HIRENASD configuration.

	Coarse Mesh	Medium Mesh	Fine Mesh
Number of nodes	1,034,003	2,448,805	7,206,319
Number of elements	1,530,645	4,003,410	13,169,981
Hexahedra	907,276	2,087,562	5,892,524
Tetrahedra	593,662	1,858,259	7,126,948
Wedges	8,554	10,128	16,588
Pyramids	21,153	47,461	133,921
First grid point @ wall, (meter)	$4.4e^{-07}$	$2.9e^{-07}$	$2.0e^{-07}$
	$(y^+ = 1.00)$	$(y^+ = 0.66)$	$(y^+ = 0.44)$
Wind-Tunnel Ceiling Boundary Cond.	Symmetry	Symmetry	Symmetry

from power spectral and cross spectral densities (PSDs and CSDs), which were computed using Welch's periodogram method. The Fourier coefficients used in computing the PSDs and CSDs were generated using discrete Fourier transform (DFT) analysis of the time histories. Overlap averaged ensembles of the data sets were used for cases where more than one cycle of data was available to analyze. The length of the ensembles and the frequency, f^*, at which the data was extracted were chosen based on statistical analysis of the results of varying the ensemble lengths. The objective in varying the block size was to exactly match the system frequency with a Fourier analysis frequency and then maximize the number of data blocks to reduce the processing-based uncertainty. The block size for the final analysis was determined by minimizing the standard deviation among the periodograms of the peak of the PSD. In general, this gives slightly different frequency selection than would be obtained by a selection of the peak value of the PSD. In all cases, a rectangular window was used; the windows were overlapped by 90% of the block size.

The displacement quantity, or reference signal, for HIRENASD, was the chord-normalized vertical displacement at accelerometer 15, Figure 1b. The magnitudes of its FRFs to be presented are shown as:

$$\left| \frac{C_p}{\frac{z}{c}} \left(f^* \right) \right| vs. \frac{x}{c} \tag{12}$$

6 COMPUTATIONAL RESULTS

6.1 Rigid-body and Static-Aeroelastic Computational Results

The aeroelastic solution process requires that the rigid body steady solutions be obtained first. These solutions are then used as initial conditions for the corresponding static aeroelastic solutions. The aerodynamic coefficients obtained from both the rigid steady and static aeroelastic calculations for the coarse, medium, and fine grids are shown in Table 3. The static aerodynamic coefficients are plotted as a function of grid factor in Figure 4. The 'N' in these plots represents number of grid points. In this figure, gray diamonds represent values submitted to AePW by all participants. The colored symbols
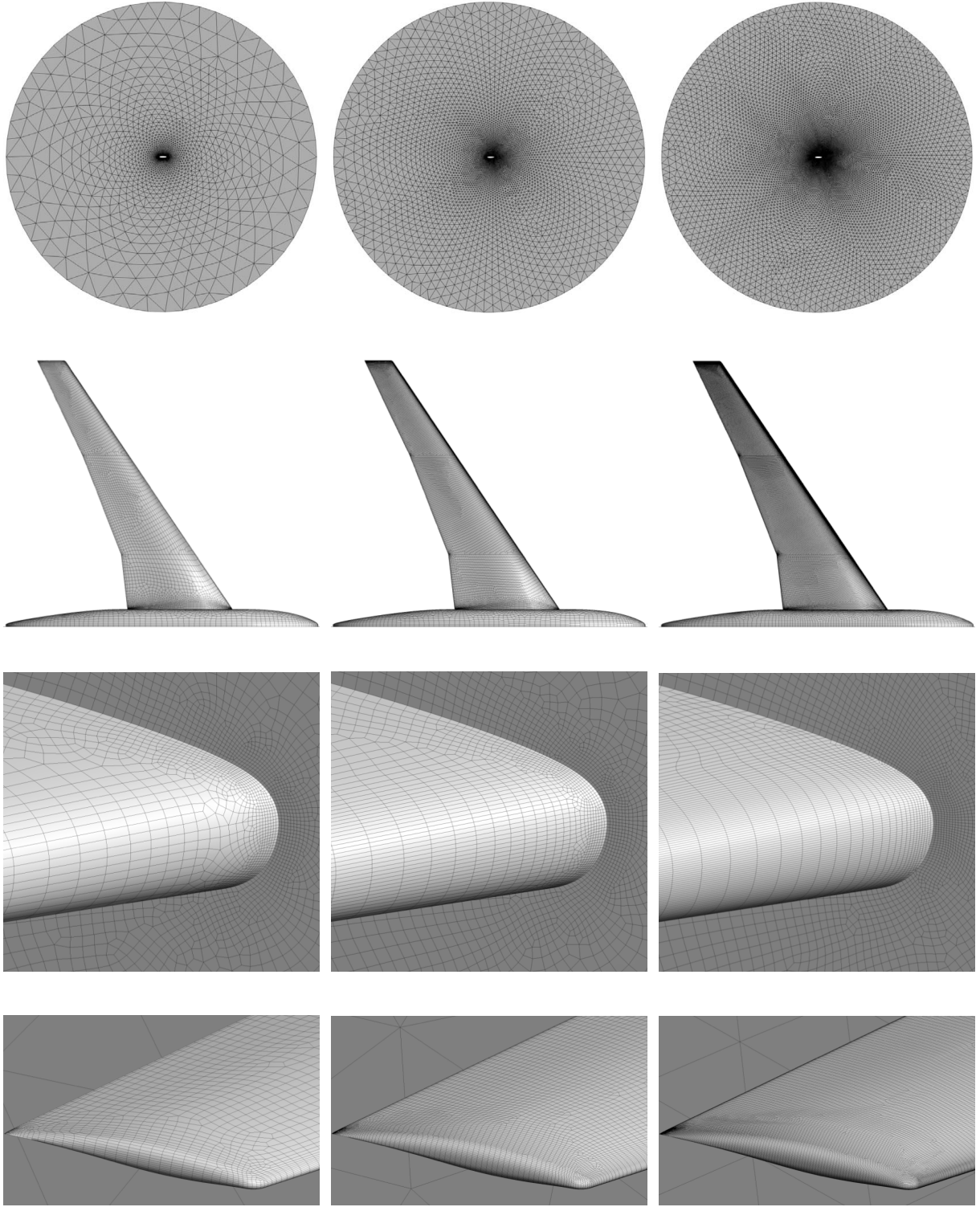
(a) Coarse Mesh   (b) Medium Mesh   (c) Fine Mesh

Figure 3: HIRENASD Solar Mesh: Symmetry Plane, Wing Planform, Leading Edge, and Wing Tip.

and lines are obtained from the post-workshop computations. These results show that the solutions from four solvers converge in the direction of the common values. They are

also more tightly clustered than the AePW values. An additional finer grid(s) study is necessary to determine further trends in solution dependence on grid refinement.

Figures 5 and 6 present C_p results at all seven wing span stations and compare the results with the experimental data on the lower and upper wing surfaces. In these figures, colored lines represent the computational data produced in the current study. The red, blue, and orange lines correspond to coarse, medium, and fine grid solutions from all four flow solvers. The background gray color represents the 24 data sets submitted by the AePW participants. Black circles represent the mode of the experimental data, which is the value that appears most often in the experimental set of data. The triangular black symbols, which are omitted from the legends, show the minimum and the maximum values in the experimental data. It is clear from these figures that the common grid and the same turbulence model analyses bring the computational data closer together when compared to AePW computational results database. Figure 7 provides a zoomed in view of the shock region on the upper surface and the peak pressure region on the lower surface at station 4. In addition, this figure identifies each flow solver. For clarity purposes, the symbols identifying experimental data (mode, minimum, and maximum values) were changed to yellow color with a black border. Several conclusions can be drawn from these figures: (1) None of the flow solver results perfectly match the experimental data, (2) The medium and fine grid solutions are tightly grouped on the upper surface and are closer to the experimental data than the coarse grid solution, (3) there is a large scatter in results on the upper surface across the shock region; however, the medium and fine grid solutions more closely resemble the experimental shock shape than the coarse grid solution.

Table 3: Computed Aerodynamic Coefficients for Coarse/Medium/Fine Meshes (Rigid Steady and Static Aeroelastic Solutions), Mach = 0.8, Re = 7 million.

	C_L			C_D			C_M		
	Coarse	Medium	Fine	Coarse	Medium	Fine	Coarse	Medium	Fine
Fluent Rigid	0.36520	0.35967	0.35839	0.01703	0.01556	0.01507	-0.30651	-0.30161	-0.29917
Fluent Static	0.34607	0.33994	0.33896	0.01618	0.01470	0.01416	-0.28779	-0.28225	-0.28007
TAU Rigid	0.36722	0.35347	0.35421	0.01538	0.01457	0.01436	-0.30689	-0.29477	-0.29498
TAU Static	0.34899	0.33616	0.33671	0.01461	0.01387	0.01366	-0.28928	-0.27812	-0.27826
Edge Rigid	0.34491	0.34378	0.34826	0.01418	0.01405	0.01401	-0.28419	-0.28505	-0.28901
Edge Static	0.32688	0.32632	0.32998	0.01352	0.01340	0.01338	-0.26772	-0.26890	-0.27229
FUN3D Rigid	0.35898	0.35219	0.35422	0.01636	0.01508	0.01475	-0.30200	-0.29343	-0.29496
FUN3D Static	0.34073	0.33431	0.33617	0.01561	0.01437	0.01405	-0.28264	-0.27627	-0.27771
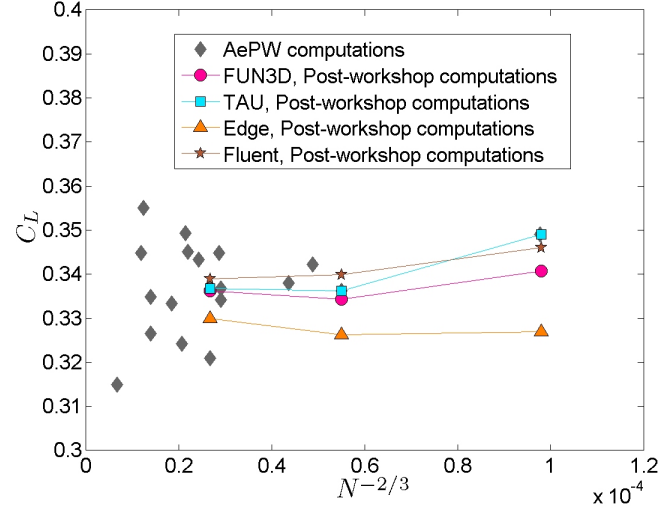
(a) Lift Coefficient.
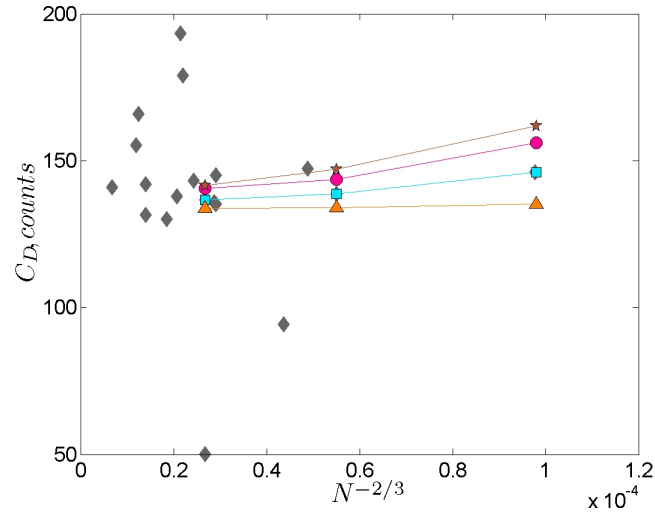
(b) Drag Coefficient.
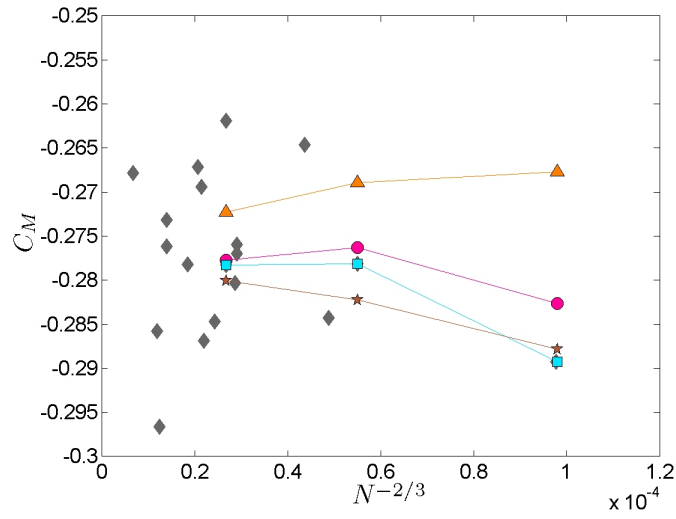
(c) Pitching Moment Coefficient.

Figure 4: Aerodynamic Coefficients from Static Aeroelastic Solutions.
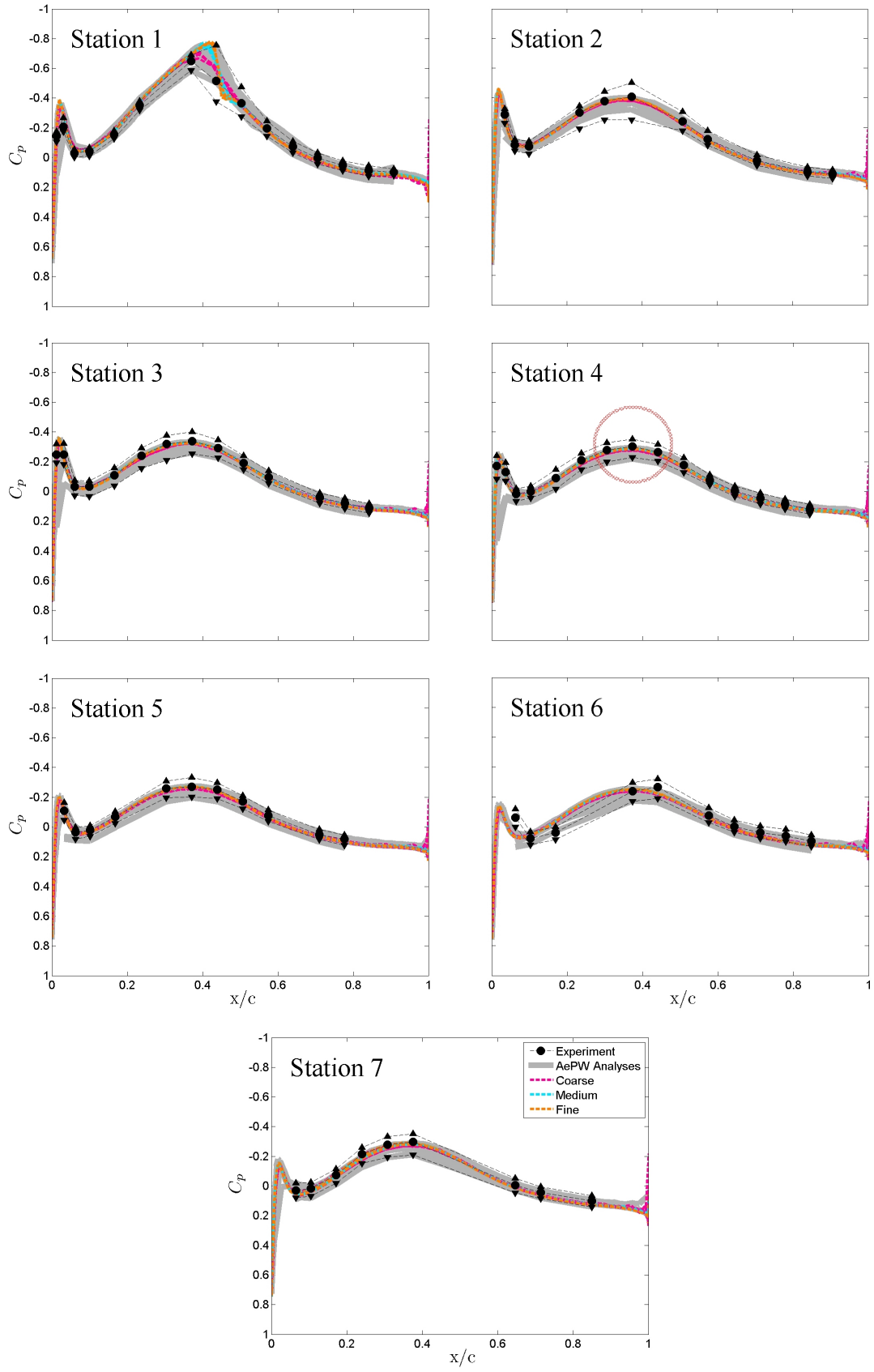
14

Figure 5: Static aeroelastic solution: C_p for coarse/medium/fine grids on lower wing's surface.
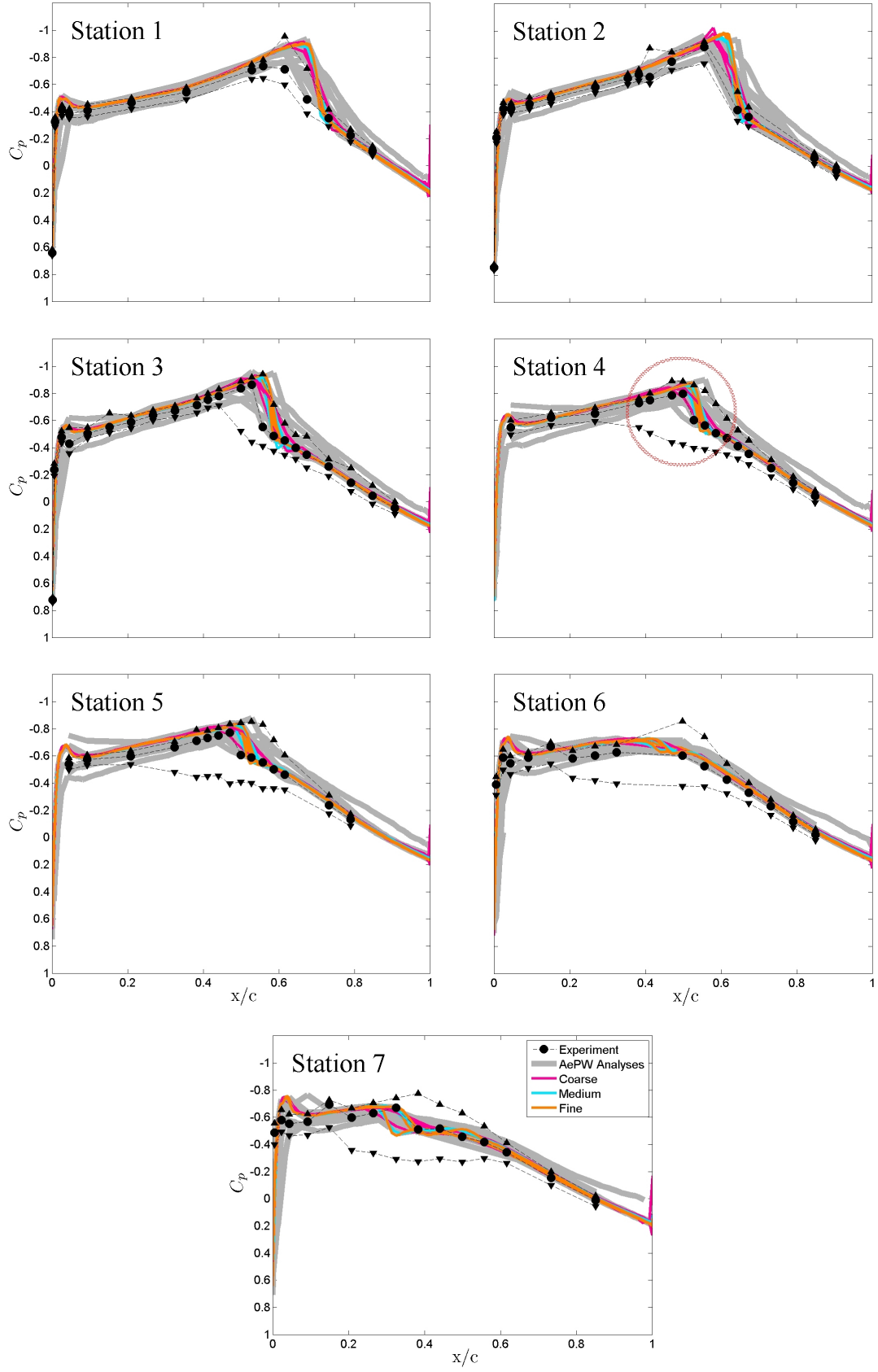
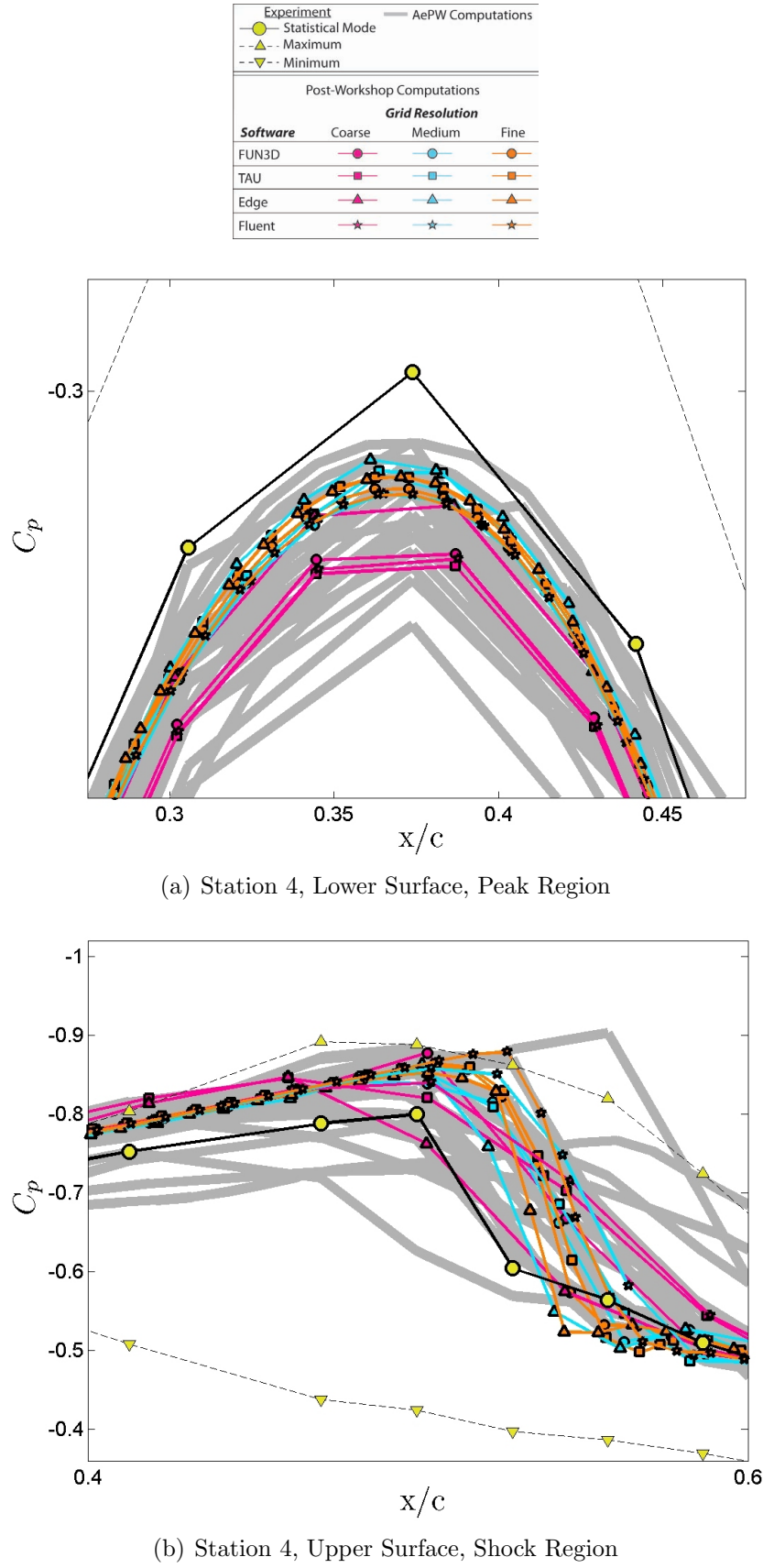Figure 6: Static aeroelastic solution: C_p for coarse/medium/fine grids on upper wing's surface.

(a) Station 4, Lower Surface, Peak Region

(b) Station 4, Upper Surface, Shock Region

Figure 7: TAU, Edge, Fluent, FUN3D static aeroelastic solution: C_p for coarse/medium/fine grids at station 4 zoomed in on peak values (lower surface) and shock region (upper surface).

6.2 Forced Excitation Analysis

The results presented here were obtained using the TAU, Edge, and FUN3D flow solver. The Fluent flow solver results were not obtained in time for this publication and will be published in the future.

The HIRENASD experimental forced excitation tests were conducted to measure the interaction between the aerodynamics and the moving wing. The forcing frequency in this study is 78.9 Hz as presented in Table 1. Numerically, the motion of the wing is accomplished via modal excitation using either equation 7 or 11. The unsteady simulations were performed by restarting computations from the static aeroelastic solutions. Typically, two to four cycles of solutions are run before the surface pressure data on the entire wing are collected at each time step. Detailed analysis of the effects of number of cycles or convergence criteria on time accurate solutions are not addressed here. After the surface pressure data were collected, each participant in this study used their own software to generate cutting planes at seven span stations to extract pressure coefficient as a function of a local chord length at each time step. These pressure time histories were then sent to one person to generate the FRFs of pressure due to displacements as described in Section 5.1. The displacement location coincided with the location of accelerometer 15. The displacement value was normalized by the reference chord. Figures 8, 9, 11, and 12 show the resulting C_p magnitude and phase plots for the upper and lower surfaces, for wing stations 1 through 7 for the coarse, medium, and fine grids for all flow solvers. Figures 10 and 13 show zoomed in views at Station 4. The results from the three flow solvers are grouped more closely together than the results in the AePW database. The detailed label of the magnitude of the FRFs is in the corresponding plots. The phase label was omitted from the plots, but its detailed meaning is $\phi(C_p/(z/\bar{c})^\circ at f^*$.
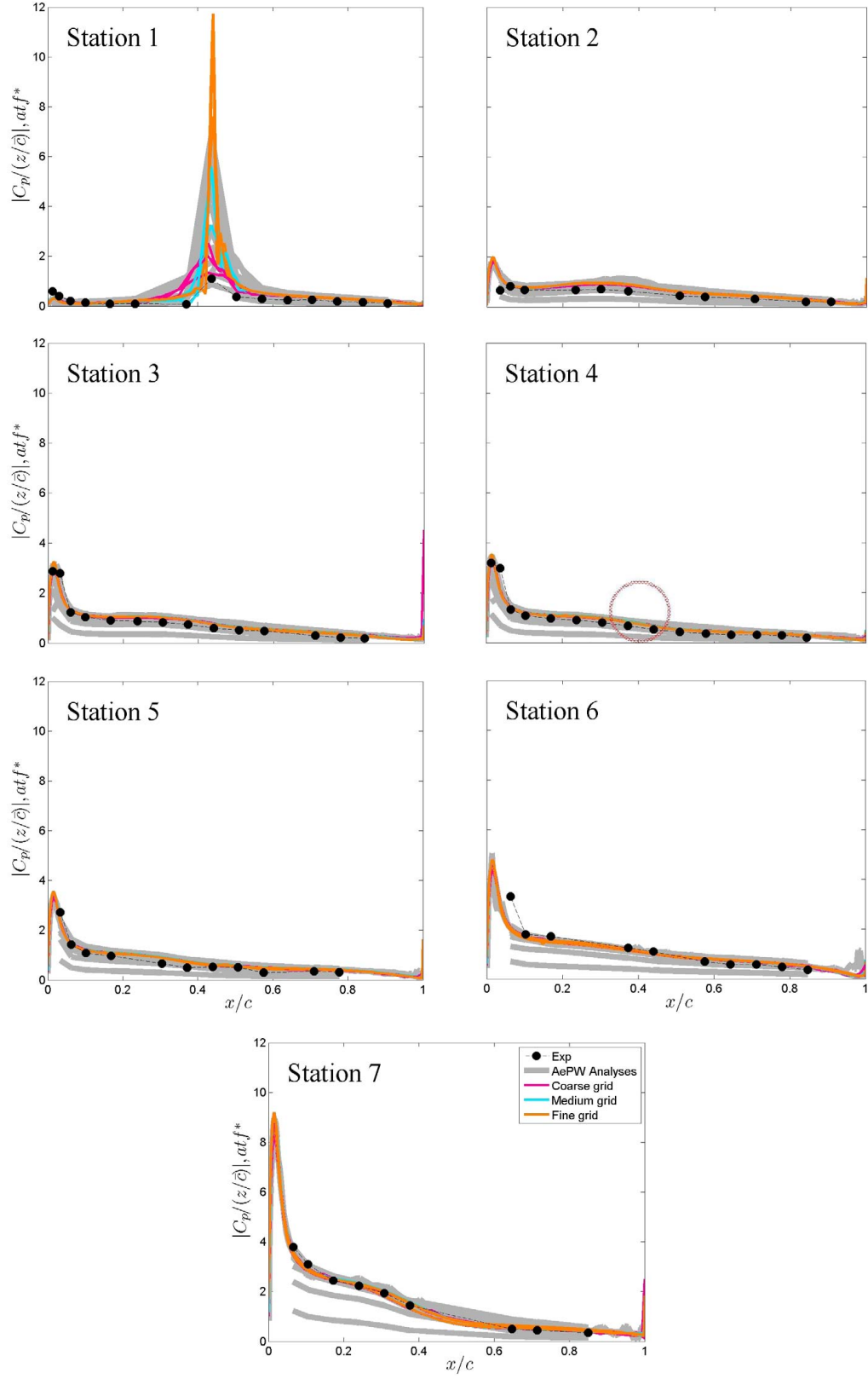
Figure 8: Magnitudes of the FRFs of the pressure coefficient due to the displacement at accel. 15 for coarse/medium/fine grids on the lower surface; Mach = 0.8, Re = 7 million.
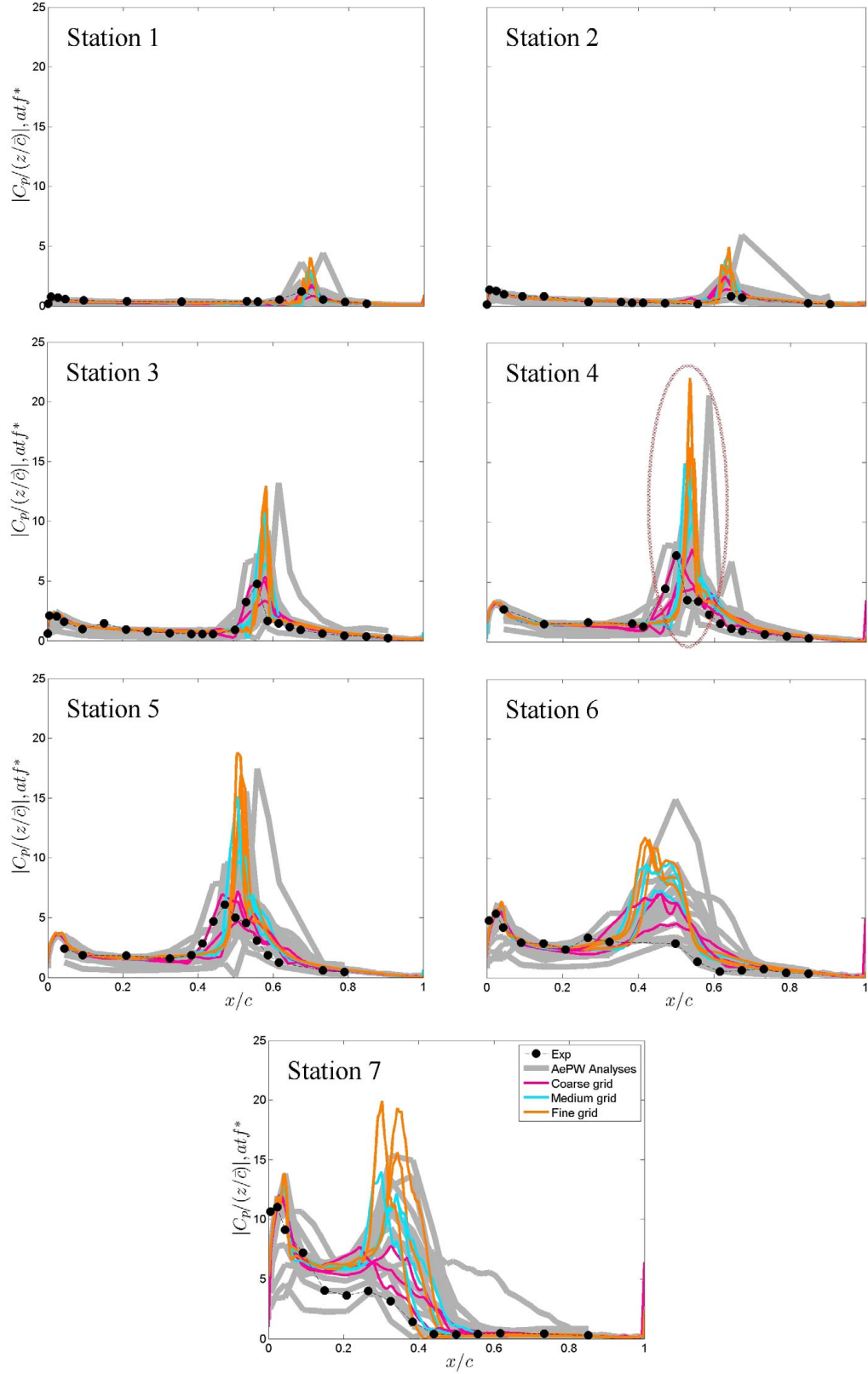
Figure 9: Magnitudes of the FRFs of the pressure coefficient due to the displacement at accel. 15 for coarse/medium/fine grids on the upper surface; Mach = 0.8, Re = 7 million.
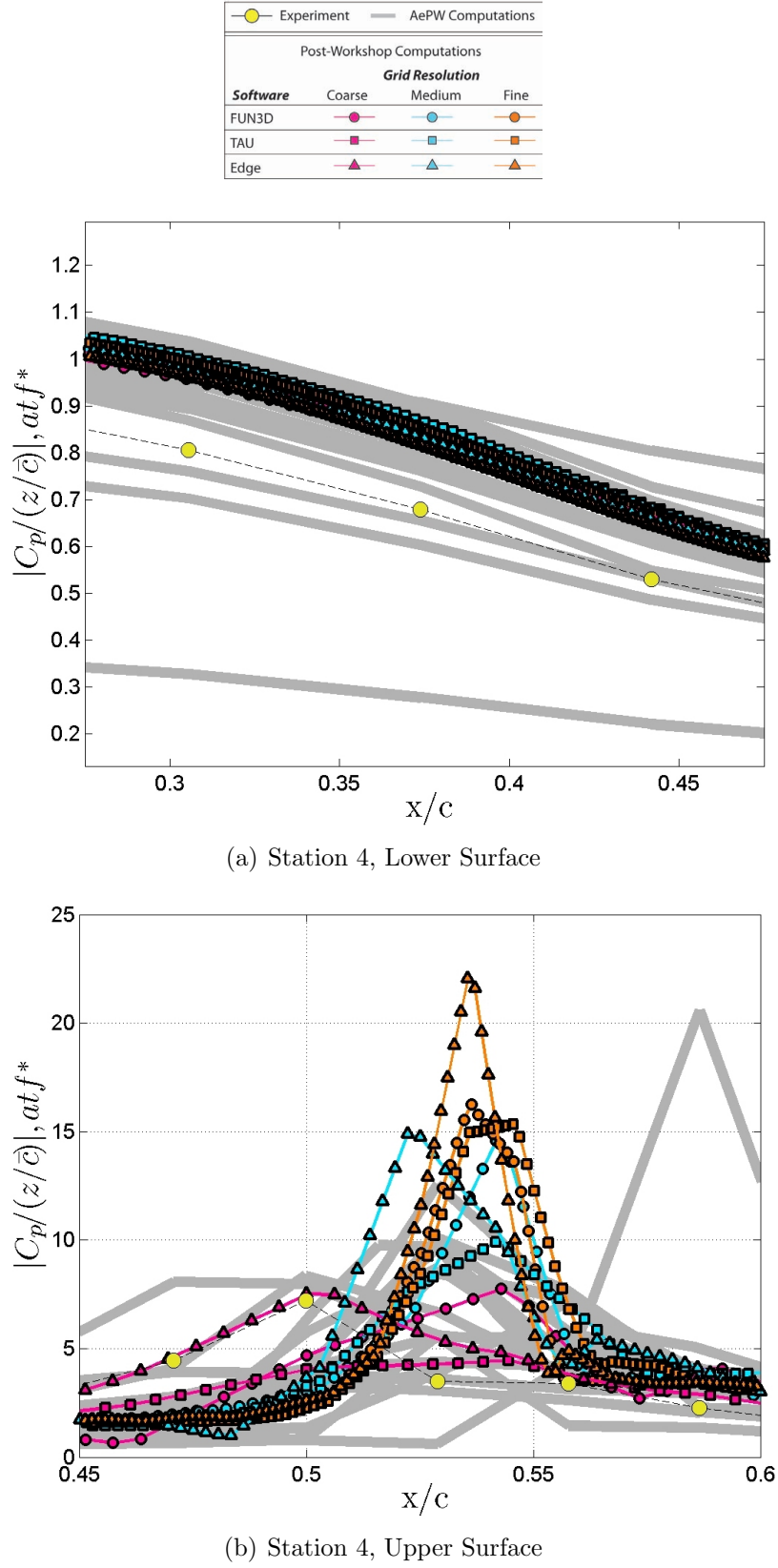
(a) Station 4, Lower Surface

(b) Station 4, Upper Surface

Figure 10: TAU, Edge, FUN3D solutions: Magnitude of FRFs for coarse/medium/fine grids at station 4 zoomed in on lower and upper surfaces.
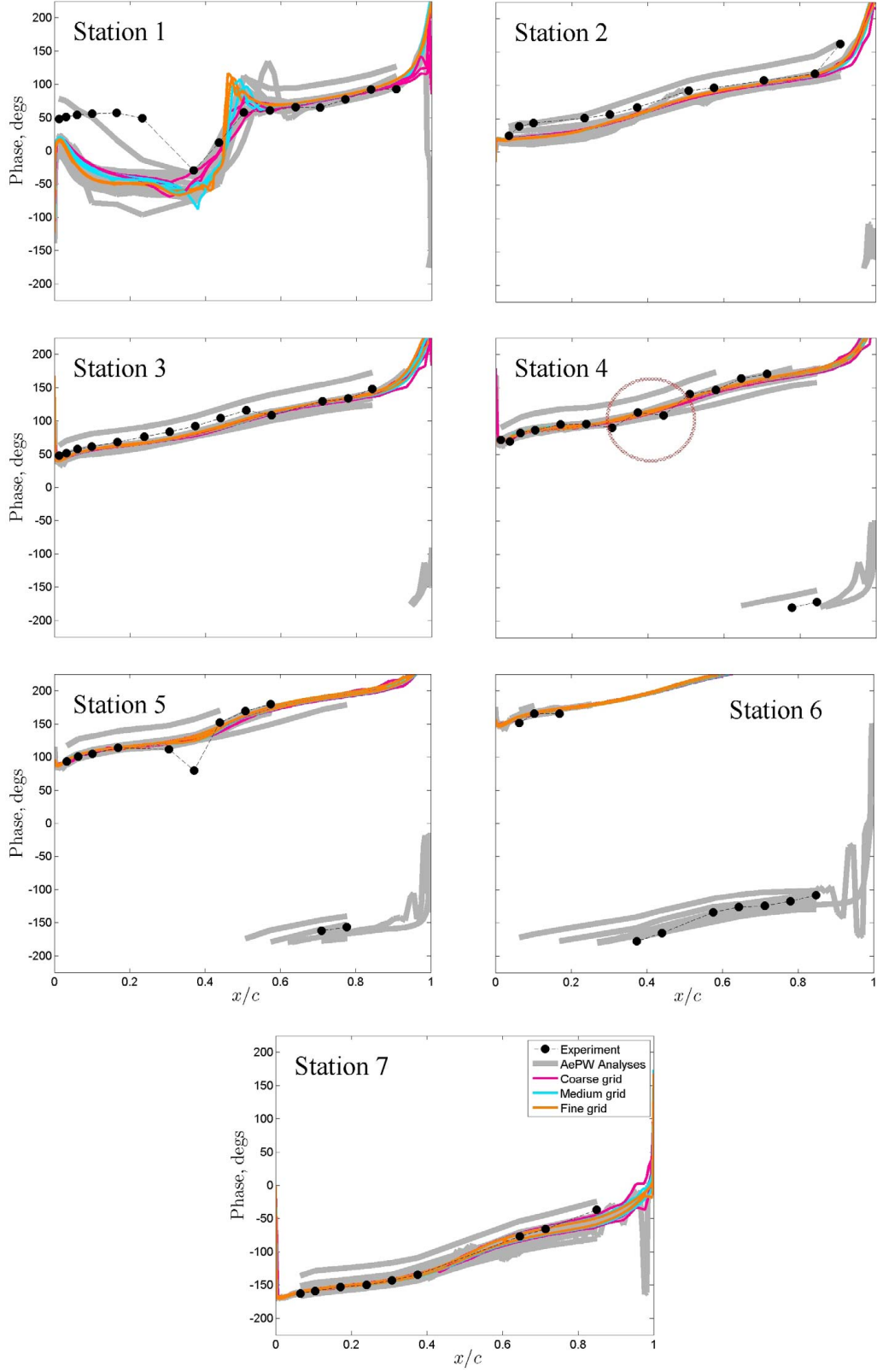
Figure 11: Phase of the FRFs of the pressure coefficient due to the displacement at accel. 15 for coarse/medium/fine grids on the lower surface; Mach = 0.8, Re = 7 million.
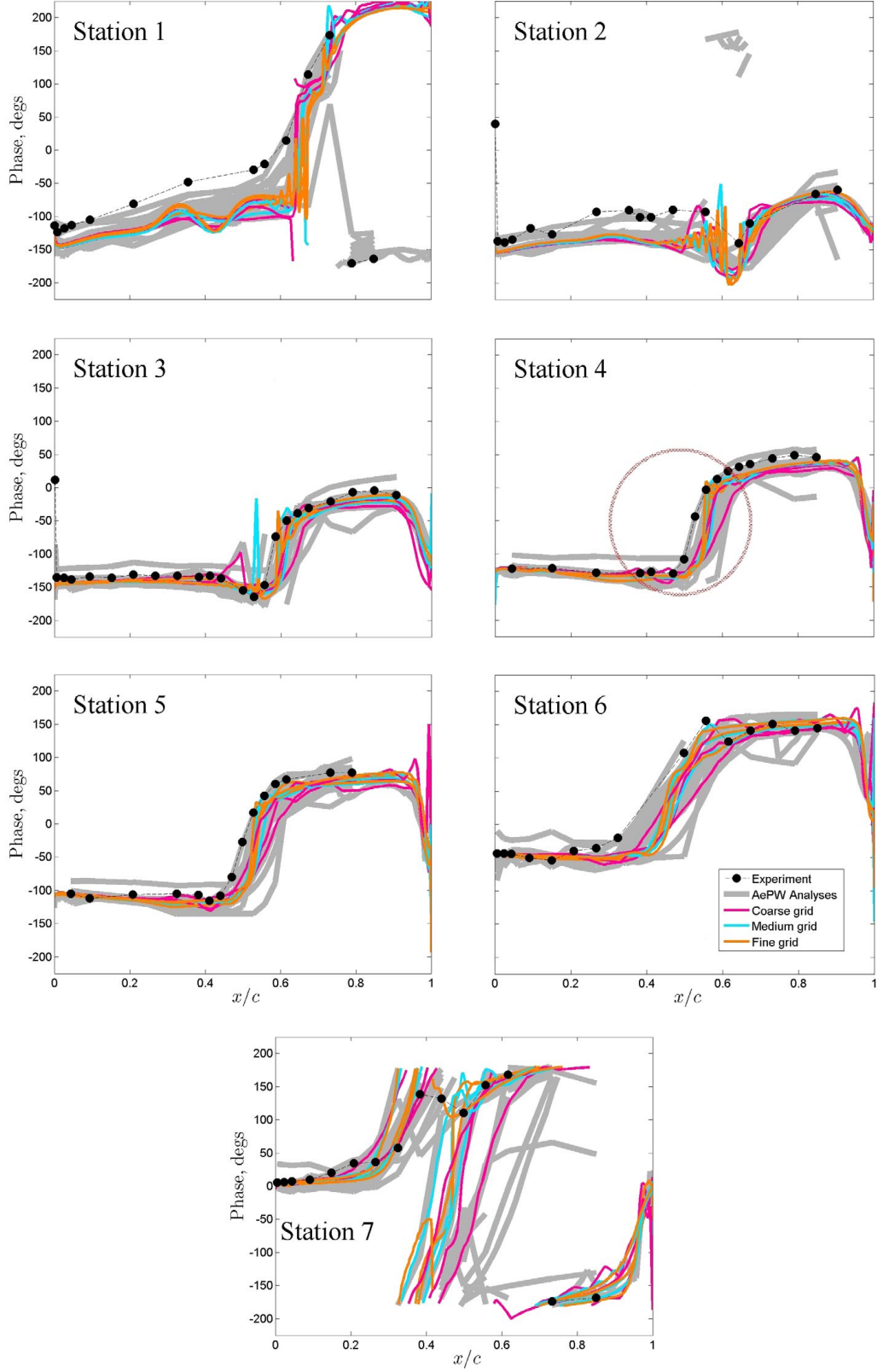
Figure 12: Phase of the FRFs of the pressure coefficient due to the displacement at accel. 15 for coarse/medium/fine grids on the upper surface; Mach = 0.8, Re = 7 million.
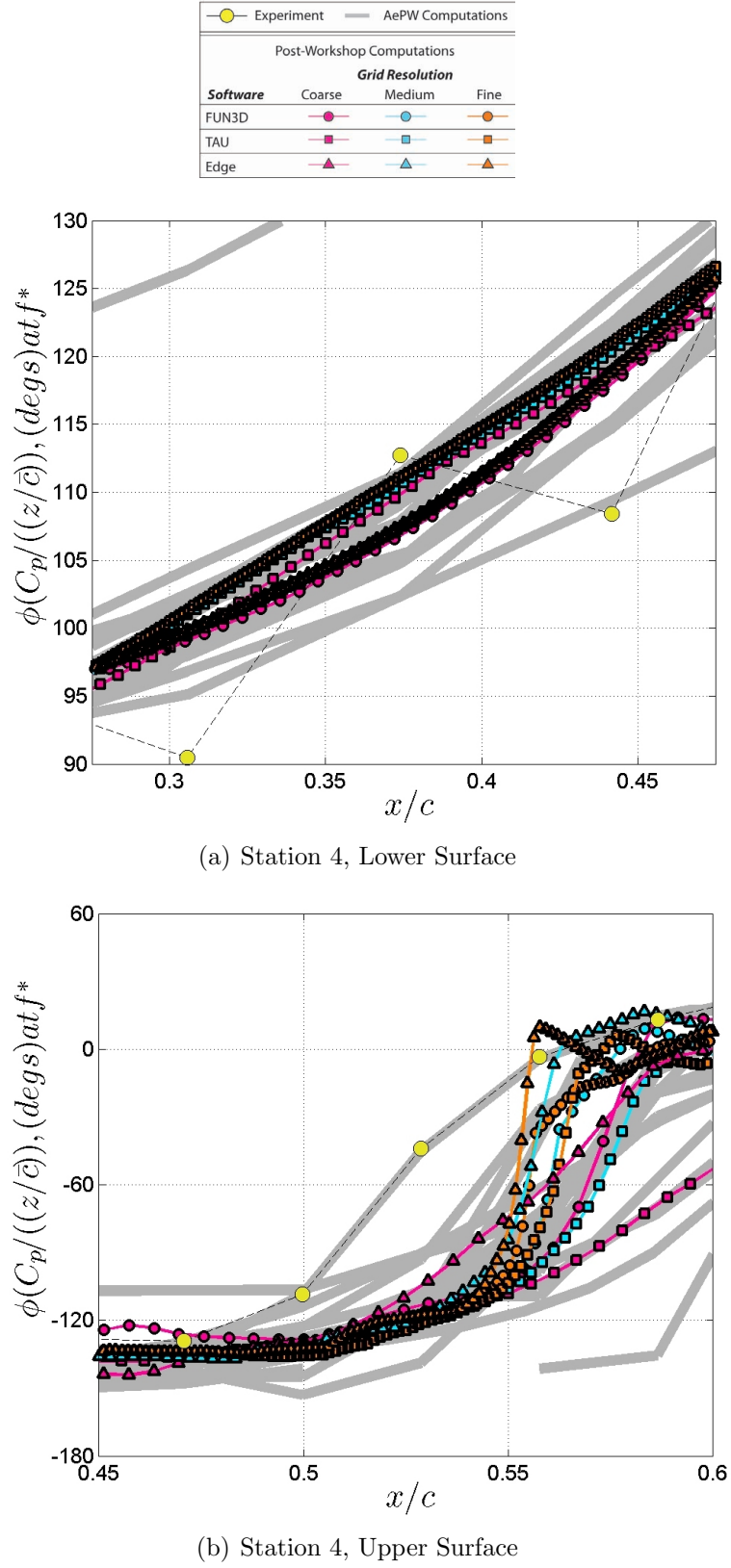
(a) Station 4, Lower Surface

(b) Station 4, Upper Surface

Figure 13: TAU, Edge, FUN3D solutions: Phase of FRFs for coarse/medium/fine grids at station 4 zoomed in on lower and upper surfaces.

24

## 6.3 Post Processing Issues

The first attempt at computing FRFs from the time histories at each span station obtained from each flow solver produced small spikes on both upper and lower surfaces. An example is presented in Figure 14a at Station 2. Station 2 is used as an example only, but these spikes were present at other stations too. Figure 14b presents the zoomed in region indicated in Figure 14a by the black circle. Note, that in these figures the x-axis has not been normalized by the chord. The cause of these spikes was traced back to the point distribution obtained from the cutting planes at each stations. Due to the orientation of the quadrilateral elements on the surface with respect to the cutting plane, every third or fourth point in the extracted plane is very close to another point. Figure 14c shows the fine grid with a cutting plane in red color at Station 2 on the lower wing surface. Six locations marked in green show examples where the cutting plane's grid points are very close to each other. These six locations are repeated in Figure 14b together with the spikes in FRFs. To mitigate this issue, the cutting plane's grid distribution and its corresponding pressure coefficient values were re-distributed using linear interpolation. The linear interpolation was consistent among three flow solvers. The point distribution after the interpolation is not shown here, but the FRF's presented in Figures 8, 9, 11, and 12 were generated on the interpolated point distribution.

Figure 15 presents another example why in this study we are insisting on a same-software and a same-person post processing analysis. In this figure, in orange color, the FRFs were produced from a linearly interpolated point distribution as described in the previous paragraph. The blue color line represents the FRFs calculated by one of the AePW participant in preparation for that workshop. The results show some differences in peak values. The pink line was derived from the blue line after additional spline interpolation to extract the C_p values at the experimental pressure tab locations. Yet, another difference among interpolated values is noticeable.

It is also clear from Figure 15 that the extraction of the pressure coefficients at the experimental tab location does not capture the shock shape produced by FRFs. The resolution of the experimental pressure tabs is too coarse.

Another conclusion can be drawn from the above post processing analysis. The same-software and the same-person post processing should start from the pressure time histories of the entire wing surfaces and not from the pressure time histories of already extracted and perhaps splined data by each researcher. This in turn would eliminate differences between the extraction of pressure at each span station and the differences in splining methods to redistribute the pressure at each station.

(a) Magnitude of FRFs.

(b) Magnitude of FRFs - zoomed in.
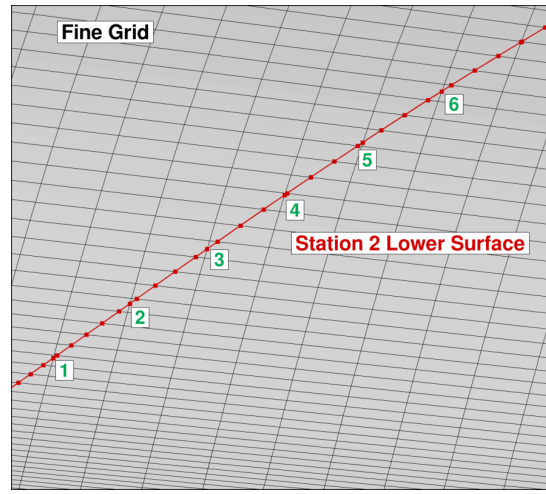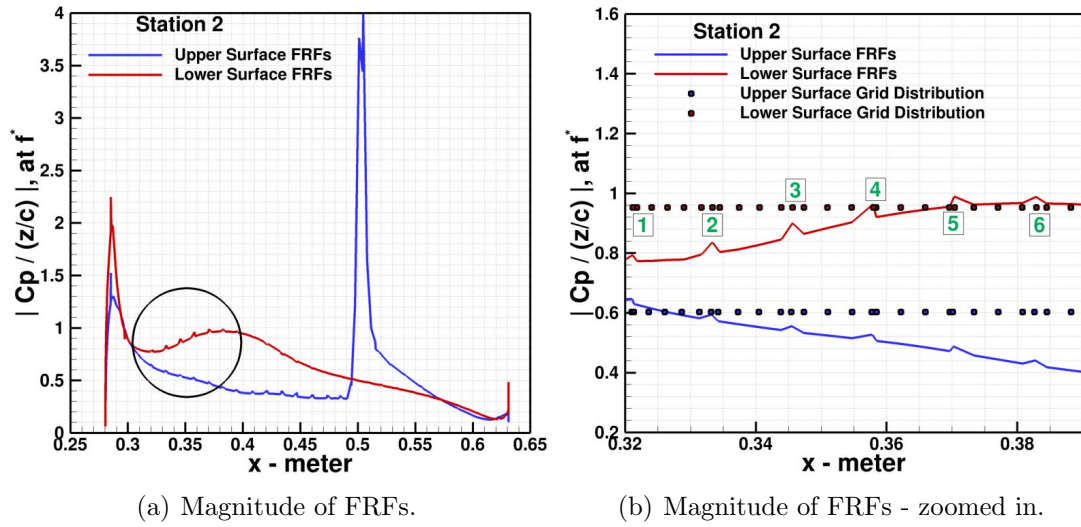
(c) Grid Distribution vs. Cutting Plane.
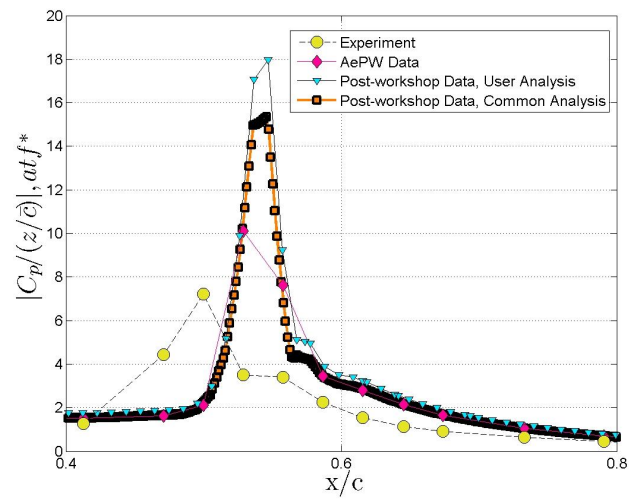
Figure 14: Grid Distribution and FRFs spikes.

Figure 15: AePW and post AePW FRFs processing, Station 4 upper surface.

7 CONCLUDING REMARKS

The HIRENASD configuration analysis using a common grid, same turbulence model, and the same post processing methods produced much lower spread in the computational results. The computed aerodynamic coefficients converge in the same directions and are more closely spaced than the AePW database. The pressure coefficients at all stations are also very close to each other. The magnitude and phase of the frequency response functions of the pressure coefficient due to normalized deflection showed less spread when compared to the AePW database.

The results from this study did not, in general, produce computational results that are significantly closer to the experimental data. Further grid refinement, temporal refinement studies, and parametric uncertainty assessments are recommended.

8 REFERENCES

[1] Heeg, J., Ballmann, J., Bhatia, K., et al. Plans for an Aeroelastic Prediction Workshop. IFASD Paper 2011-110.

[2] Heeg, J., Chwalowski, P., Florance, J. P., et al. (2013). Overview of the Aeroelastic Prediction Workshop. AIAA-2013-0783, 51st AIAA Aerospace Sciences Meeting including The New Horizons Forum and Aerospace Exposition, Grapevine, Texas, 7-10 Jan., 2013.

[3] Heeg, J., Chwalowski, P., Schuster, D. M., et al. (2013). Overview and Lessons Learned from the Aeroelastic Prediction Workshop. AIAA-2013-1798, 54th AIAA/ASME/ASCE/AHS/ASC Structures, Structural Dynamics, and Materials Conference, Boston, Massachusetts, Jan. 8-11, 2013.

[4] http://aaac.larc.nasa.gov/tsab/cfdlarc/aiaa-dpw/. August 2010.

[5] http://hiliftpw.larc.nasa.gov/. August 2010.

[6] Morrison, J. H. and Hemsch, M. J. (2007). Statistical Analysis of CFD Solutions from the First AIAA Drag Prediction Workshop. AIAA-2007-254, 45th AIAA Aerospace Sciences Meeting and Exhibit, Reno, Nevada, 8-11 Jan., 2007.

[7] Park, M. A., Laflin, K. R., Chaffin, M. S., et al. (2013). CFL3D, FUN3D, and NSU3D Contributions to the Fifth Drag Prediction Workshop. AIAA-2013-0050, 51st AIAA Aerospace Sciences Meeting including The New Horizons Forum and Aerospace Exposition, Grapevine, Texas, 7-10 Jan., 2013.

[8] Spalart, P. R. and Allmaras, S. R. A One-Equation Turbulence Model for Aerodynamic Flows. *La Recherche Aerospatiale*, No. 1, 1994, pp 5–21.

[9] Schwamborn, D., Gerhold, T., and Heinrich, R. The DLR TAU-CODE: Recent Applications in Research and Industry. Technical Report at European Conference on Computational Fluid Dynamics. ECCOMAS CFD 2006.

[10] http://tau.dlr.de/. Description of the DLR TAU code, March 2012.

[11] Eliasson, P. (2002). EDGE, a Navier-Stokes solver for unstructured grids. In *Proc. to Finite Volumes for Complex Applications III*. ISBN 1 9039 9634 1, pp. 527–534.

[12] Weiss, J. M., Maruszewski, J. P., and Smith, W. A. (1999). Implicit Solution of Preconditioned Navier-Stokes Equations Using Algebraic Multigrid. AIAA Journal, Vol. 37, No. 1, January 1999.

[13] http://fun3d.larc.nasa.gov. NASA Langley Research Center, November 2010.

[14] http://www.dlr.de/sc/en/desktopdefault.aspx/. Information about the Flow Simulator, DLR, March 2012.

[15] Neumann, J. and Ritter, M. Steady and Uunsteady Aeroelastic Simulations of the HIRENASD Wind Tunnel Experiment. IFASD Paper 2009.

[16] Eliasson, P., Nordströom, J., and Weinerfelt, P. (2009). Application of a Line-Implicit Scheme on Stretched Unstructured Grids. AIAA-2009-163, 47th AIAA Aerospace Sciences Meeting including The New Horizons Forum and Aerospace Exposition, Orlando, Florida, 5-8 Jan., 2009.

[17] Roe, P. L. Approximate Riemann Solvers, Parameter Vectors, and Difference Schemes. *Journal of Computational Physics*. Vol. 43, No. 2, 1981.

[18] http://www.rbf morph.com/. RBF Morph.

[19] Biancolini, M. E. (2013). Mesh Morphing and Smoothing by Means of Radial Basis Functions (RBF): A Practical Example Using Fluent and RBF Morph. Handbook of Research on Computational Science and Engineering: Theory and Practice, IGI Global, (in press).

[20] Venkatakrishnan, V. Convergence to Steady State Solutions of the Euler Equations on Unstructured Grids with Limiter. *Journal of Computational Physics*. Vol. 118, No. 1, 1995.

[21] Biedron, R. T. and Thomas, J. L. Recent Enhancements to the FUN3D Flow Solver for Moving-Mesh Applications. AIAA-2009-1360, 47th AIAA Aerospace Sciences Meeting including The New Horizons Forum and Aerospace Exposition, Orlando, Florida, 5-8 Jan., 2009.

[22] Biedron, R. T. and Lee-Rausch, E. M. Rotor Airloads Prediction Using Unstructured Meshes and Loose CFD/CSD Coupling. AIAA Paper 2008-7341.

[23] Batina, J. T., Seidel, D. A., Bland, S. R., et al. Unsteady Transonic Flow Calculations for Realistic Aircraft Configurations. AIAA Paper 1987-0850.

[24] Bartels, R. E., Rumsey, C. L., and Biedron, R. T. CFL3D Version 6.4 - General Usage and Aeroelastic Analysis. NASA TM 2006-214301 March 2006.

[25] https://heinrich.lufmech.rwth-aachen.de/en/. Aachen University, June 2010.

[26] Wieseman, C., Chwalowski, P., and Heeg, J. (2013). Structural Dynamics Modeling of HIRENASD in Support of the Aeroelastic Prediction Workshop. AIAA-2013-1801, 54th AIAA/ASME/ASCE/AHS/ASC Structures, Structural Dynamics, and Materials Conference, Boston, Massachusetts, Jan. 8-11, 2013.

[27] Leatham, M., Stokes, S., Shaw, J. A., et al. Automatic Mesh Generation for Rapid-Response Navier-Stokes Calculations. Fluids 2000, Conference and Exhibit, June 2000.